Universal Patterning for 2D Van der Waals Materials via Direct Optical Lithography

Seong Rae Cho, Seonghun Ahn, Seung Hyung Lee, Heonhak Ha, Tae Soo Kim, Min-kyung Jo, Chanwoo Song, Tae Hong Im, Pragya Rani, Minseung Gyeon, Kiwon Cho, Seungwoo Song, Min Seok Jang,* Yong-Hoon Cho,* Keon Jae Lee,* and Kibum Kang*

Advanced patterning techniques are essential to pursue applications of 2D van der Waals (vdW) materials in electrical and optical devices. Here, the direct optical lithography (DOL) of vdW materials by single-pulse irradiation of high-power light through a photomask is reported. The DOL exhibits large-scale patterning with a sub-micrometer resolution and clean surface, which can be applied to various combinations of vdW materials and substrates. In addition, the thermal profile during DOL is investigated using the finite element method, and the ideal conditions of DOL according to the materials and substrates are determined.

1. Introduction

Patterning is a crucial process that determines the electrical and optical performances of devices. Recently, 2D van der Waals (vdW) materials have emerged, and the development of their patterning process is important.[1–3] However, photoresist-based conventional photolithography (CP) optimized for traditional semiconductors is still used for the patterning of vdW materials,[4,5] which significantly affects the performance of ultrathin vdW materials due to the polymer residue and reactive chemical solvent.[6–9] Therefore, a customized patterning technique for 2D vdW materials that utilize the characteristics of 2D vdW materials is in high demand. In this regard, various patterning techniques of 2D vdW materials have been considered so far. The reported patterning techniques, however, suffer from critical drawbacks. For instance, selective-growth techniques exhibit low resolution or low scalability for various types of materials, since surface treatments for growth are vulnerable to lithographic processes or growth conditions are limited by the treatment.[10,11] Focused-laser writing techniques exhibit substrate dependency or low resolution due to the low energy or large beam size of the laser.[12,13] Nano-mechanical patterning methods show low throughput and local scale due to their bottom-up nature.[14,15] The patterning method customized for vdW materials with large-scale, high-throughput, and high-resolution has yet to be reported.

In this paper, we report on high-resolution and high-throughput photoresist-free direct optical lithography (DOL) via highly intense large-area photo illumination with a short pulse. An excimer laser was used as the light source to supply highly intense energy for this work. We also show that DOL is universally applicable to various types of materials and substrates. Via DOL, vdW materials such as monolayer (ML) MoS_2, bilayer (BL) MoS_2, graphene, ML WSe_2, and 2D metal-organic framework (MOF) can be directly patterned on different types of substrates, including flexible polymers and bio-compatible chitosan. The morphology and optical property changes of 2D materials were compared after the CP and DOL patterning processes. We also carried out the finite element method (FEM) simulation to investigate the thermal decomposition mechanism during the DOL process. The simulation also revealed that a highly intense photo source with a short pulse was critical for high-resolution patterning and prevention of the negative effect on patterned vdW materials.

S. R. Cho, S. H. Lee, T. S. Kim, M.-k. Jo, C. Song, T. H. Im, P. Rani, M. Gyeon, K. Cho, K. J. Lee, K. Kang
Department of Materials Science and Engineering
Korea Advanced Institute of Science and Technology (KAIST)
Daejeon 34141, South Korea
E-mail: keonlee@kaist.ac.kr; kibumkang@kaist.ac.kr
S. Ahn, Y.-H. Cho
Department of Physics and KI for the Nano Century
Korea Advanced Institute of Science
and Technology (KAIST)
Daejeon 34141, South Korea
E-mail: yhc@kaist.ac.kr
H. Ha, M. S. Jang
School of Electrical Engineering
Korea Advanced Institute of Science
and Technology (KAIST)
Daejeon 34141, South Korea
E-mail: jang.minseok@kaist.ac.kr
M.-k. Jo, S. Song
Operando Methodology and Measurement Team
Interdisciplinary Materials Measurement Institute
Korea Research Institute of Standards
and Science (KRISS)
Daejeon 34113, Korea

2. Results and Discussion

Figure 1 exhibits the multi-scale DOL of 2D vdW material that does not require photoresist and solvents. The process
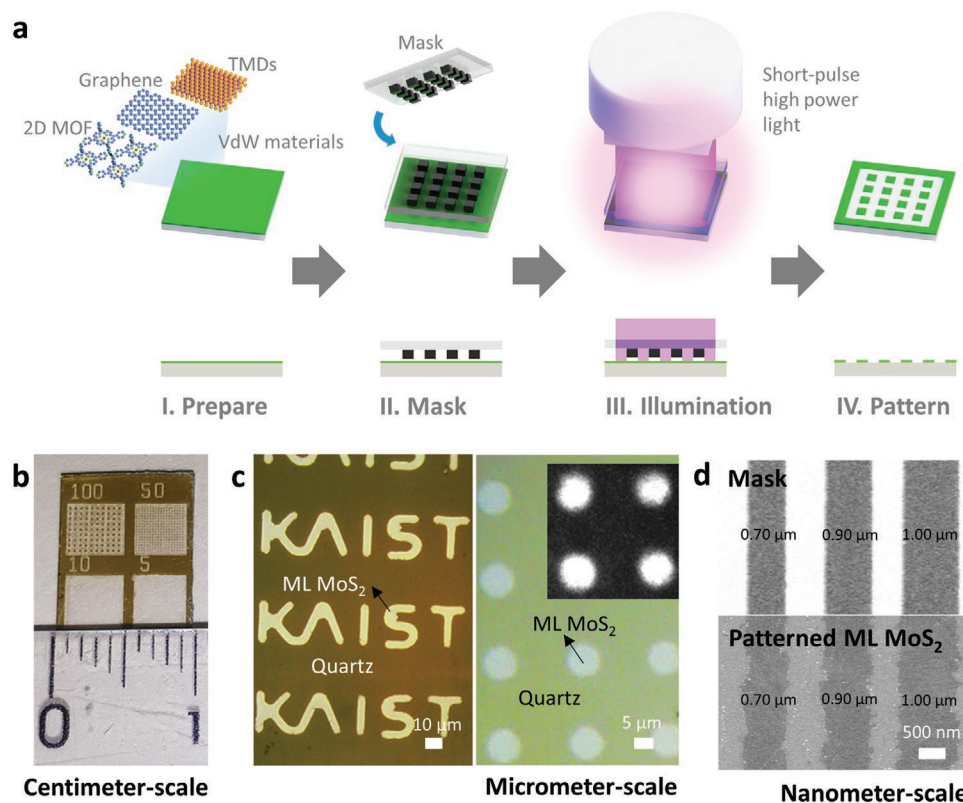
Figure 1. a) Schematic illustration of multiscale and photoresist-free direct optical lithography. b) OM image of patterned MoS_2 in centimeter scale and c) in micrometer scale with the inset of PL mapping and scale bar of 10 and 5 μm. d) SEM image of submicron-scale MoS_2 with a scale bar of 500 nm.

schematics are illustrated in Figure 1a. The as-prepared vdW materials (characterization details in Section S1, Supporting Information) were covered using a photo mask and illuminated by a highly intense photo source. The photo source penetrated the photo mask and directly etched the vdW materials following patterns of the photo mask. After illumination, the photo mask was removed, and the resultant samples were investigated (for a detailed description of the process, refer to Section 4).

Figure 1b–d shows a representative multi-scale pattern (centimeter to nanometer) using monolayer MoS_2. The large-area arrangement of ML MoS_2 patterns with radii of 100, 50, 10, and 5 μm were fabricated on a quartz substrate as presented in the centimeter-scale image (Figure 1b). The illumination beam size was 625 $μm^2$ × 625 $μm^2$ in this work, so patterning for the centimeter scale was performed via beam scanning by moving a stage. However, the beam size can be enlarged to any extent by optical lenses. The micrometer scale images in Figure 1c show that the symbol of our institute, Korea Advanced Institute of Science and Technology (KAIST), and circular patterns of ML MoS_2 with a radius of 5 μm were successfully defined, following patterns of the photo mask (see optical microscope (OM) images of the mask in Figure S4, Supporting Information). A wide-field PL image, an inset of the right image in Figure 1c, exhibits PL signals with a circular shape that is identical to the patterned ML MoS_2 in Figure 1c. This indicates that ML MoS_2 was patterned without residual MoS_2, as the monolayer MoS_2 exhibits strong PL close to 670 nm at room temperature.[16] Figure 1d shows scanning electron microscopy

(SEM) images of the mask and nano-scale patterned ML MoS_2 on a Si substrate. The submicron-scale patterning experiment was carried out with ML MoS_2 transferred on a Si substrate, not on a quartz substrate as in the other scale images, since the conducting nature of Si prevented charge accumulation which hinders the observation of submicron patterns in the SEM characterization. Widths of aluminum lines in the mask were 1.00, 0.90, and 0.70 μm from right to left, as exhibited in a previous image, and widths of line-patterned ML MoS_2 were 1.00, 0.90, and 0.70 μm from right to left as exhibited in the image given below. The resulting patterns of ML MoS_2 showed tiny differences from the mask's pattern due to the line edge roughness issue but were overall highly similar.

The DOL provides high-throughput, large-area and multi-scale processability, and high resolution without photoresist residues or solvents. In the next two figures, further demonstration with other 2D vdW materials and substrates is described and optical characterizations are carried to investigate effects of DOL and CP on vdW materials.

DOL results of various 2d materials on different types of substrates are demonstrated in **Figure 2**. Figure 2a,b represent OM images of patterned ML MoS_2 on a polyimide (PI) substrate, a widely used flexible polymer substrate. In the lower magnification image (Figure 2a), ML MoS_2 was patterned, while the PI substrate did not melt or decompose, so the PI substrate could be easily bent by fingers. The micron-scale patterns of ML MoS_2 were prepared on the substrate as shown in the higher magnification OM image (Figure 2b) and Raman spectra (Figure 2c).
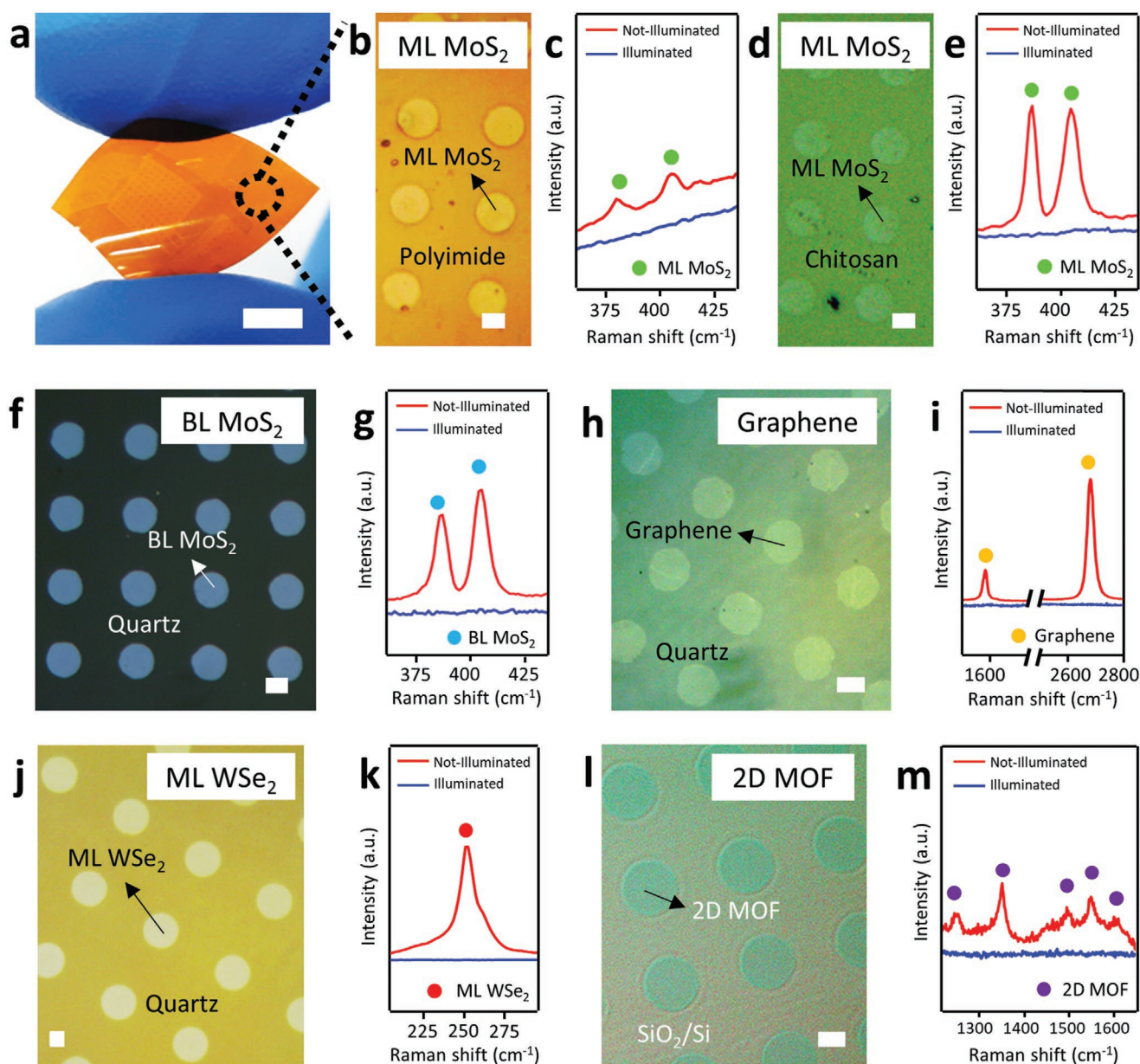
Figure 2. OM images of patterned MoS$_2$ on PI substrate with a a) scale bar of 0.5 cm and b) scale bar of 10 µm, and c) Raman spectra of patterned MoS$_2$ on PI substrate. d) OM image and e) Raman spectra of patterned ML MoS$_2$ on chitosan with a scale bar of 10 µm. f) OM image and g) Raman spectra of patterned BL MoS$_2$ on quartz with a scale bar of 10 µm. h) OM image and i) Raman spectra of patterned graphene on quartz with a scale bar of 10 µm. j) OM image and k) Raman spectra of patterned WSe$_2$ on quartz with a scale bar of 10 µm. l) OM image and m) Raman spectra of patterned MOF on SiO$_2$(300 nm)/Si substrate with a scale bar of 10 µm.

ML MoS$_2$ on a chitosan substrate, a representative biocompatible material, was patterned without damages on the substrate as well (Figure 2d,e). ML MoS$_2$ was also patterned on polydimethylsiloxane substrates (see Figure S5, Supporting Information). Polymer substrates are generally degraded or approach glass-transition temperature around or below 300 °C, which is not sufficient to entirely pattern vdW materials in a short pulse.[17–20] This is an obstacle to using the flexible nature of 2D vdW materials with flexible polymer substrates. Moreover, biocompatible materials are generally degradable in various solvents, so it limits bio application of vdW materials since

fabrication of biocompatible device through conventional process is prevented. It demonstrates that DOL is powerful for vdW material patterning on polymer and biocompatible substrates that are susceptible to heat and solvents degradation.

DOL worked not only for ML MoS$_2$, but BL MoS$_2$ on a quartz substrate was also patterned via DOL as shown in the OM image (Figure 2f). Raman spectroscopy revealed that BL MoS$_2$ was patterned without residues; characteristic peaks of BL MoS$_2$ disappeared in the illuminated regions of the Raman spectra in Figure 2g. Graphene, another representative 2D vdW material, on a quartz substrate was patterned in the shape of periodic

circles with a radius of 10 µm, as shown in Figure 2h, and therefore, it was confirmed that graphene could be exactly patterned without residues via Raman spectra (Figure 2i). ML WSe$_2$ on quartz was also patterned as shown in Figure 2j,k. Figure 2l,m indicate that the 2D MOF was patterned on a 300-nm-thick SiO$_2$/Si substrate. In particular, this reveals a huge advantage of DOL since it implies that DOL is an appropriate patterning technique for 2D vdW materials, which are sensitive to various solvents. The 2D MOFs are easily damaged by various solvents as described in Figure S6, Supporting Information, and ref. [21]. 2D MOF was removed after rinsing for 30 min in several solvents, such as, acetone, methanol, isopropyl alcohol (IPA), and distilled (DI) water. DOL does not entail a solution process during patterning. These results indicate that DOL has large scalability to solution-sensitive vdW materials, which are not compatible with solution-containing CP, as well as, general vdW materials. For comprehension of the advantages of our technique, the advantages of DOL compared to other methods are listed with respect to several important parameters in **Table 1**.

Figure 3 compares the morphology and optical properties changes of ML MoS$_2$ after the CP and DOL patterning processes to ensure the preservability of pristine properties of vdW materials of DOL compared to CP method. Through the change in the characteristics of absorption or PL, intrinsic and extrinsic properties can be identified, such as, strain, exciton binding energy, doping, and atomic defect density.[16,22–24] As mentioned in the previous section, CP forms polymeric residues on the surface of vdW materials, which degrade or modify properties of vdW materials. Figure 3a represents atomic force microscope (AFM) images of as-grown ML MoS$_2$, patterned ML MoS$_2$ through DOL, and patterned ML MoS$_2$ through CP. The surface of ML MoS$_2$ through DOL was very clean, similar to the surface of as-grown ML MoS$_2$, which did not form residues on ML MoS$_2$. However, the surface of ML MoS$_2$ through CP exhibited high roughness owing to polymeric residues caused by a polymeric photoresist. The significant amount of residues remained even after overnight lift-off process. This profile was identically observed in other spots in three samples, as high roughness from polymeric residues was observed only in the case of CP (Figure S7, Supporting Information). These polymeric residues can degrade electrical properties. I–V curves of two-terminal devices with DOL and CP BL MoS$_2$ exhibited that overall current levels of DOL samples were higher than those of CP samples (see Figure S8, Supporting Information). It is considered that contamination from polymer residues increased contact resistance of CP samples.[7]

Raman spectroscopy was examined to identify structural difference before and after each patterning (Figure 3b). Two representative Raman peaks of ML MoS$_2$, induced from in-plane (E_{2g}^1) and out-of-plane (A_{1g}) modes, were located at 386 and 407 cm^{-1} respectively, for the as-grown sample. DOL MoS$_2$ and CP MoS$_2$ have those peaks with almost the same wavenumbers and full width at half-maximum (FWHM) values, indicating that their intrinsic lattice properties were preserved after both patterning methods. Additionally, secondary Raman peak of longitudinal acoustic phonon mode, so called 2LA(M), was observed at around 453 cm^{-1} with the same FWHM in three samples. It was reported that LA(M), as well as, 2LA(M), peak was dependent on the density of defects in ML MoS$_2$.[25] 2LA(M) peak of all three samples did not show any notable difference, so additional defects of MoS$_2$ were not significantly created after both patterning methods.

Absorption of ML MoS$_2$ was measured to identify electrical properties of ML MoS$_2$ before and after each patterning method. Figure 3c shows three distinct absorption peaks, known as A, B, and C exciton absorption peaks, in all three samples. As-grown MoS$_2$ samples exhibited A, B, and C exciton absorption peaks at 1.876, 2.020, and 2.863 eV, respectively. In case of the DOL sample, peak position of A, B, and C exciton were located at similar value to those of as-grown MoS$_2$ with only few meV difference, which might be caused by strain relaxation or possible sample-to-sample variation.[26] Meanwhile, absorption peaks of CP MoS$_2$ exhibited different aspect. Peak positions of A, B, and C peaks were 1.861, 2.009, and 2.845 eV, respectively, showing red shifts with tens of meV amount in all peaks.

PL was measured to investigate emission property at room temperature in air ambient (Figure 3d). PL spectrum of as-grown MoS2 exhibited emission peak at 1.826 eV, at withstandard deviation of 8 meV at different positions. In the DOL sample, no significant difference with the as-grown sample in PL intensity was observed and small peak shift was observed, which was in a range of peak position distribution of PL profiles in the as-grown MoS$_2$ sample. Whereas, PL intensity of the CP sample was almost 3 times smaller than that of the other two samples. Therefore, optical properties of MoS$_2$ are well-preserved after DOL patterning compared to CP process. Physical origins of absorption and PL variations are discussed detail in Section S1, Supporting Information. To ensure that these optical effects generally occurred, multipoint material characterizations in Raman spectroscopy, AFM, and PL were performed as shown in Figure S11, Supporting Information.

Table 1. Important parameters comparison of DOL with similar methods.

	High throughput	Pretreatment	Resolution	Scalability to type of substrates	Scalability to type of materials
[10]	o	o	Photolithography resolution (≈2 µm)	–	–
[11]	o	o	≈50 µm	–	–
[12]	x	o	≈1 µm	x	–
[13]	x	x	≈1 µm	–	–
[14]	x	o	≈50 nm	x	–
[15]	x	o	<100 nm	–	–
This work	o	x	Photolithography resolution (≈600 nm)	o	o

**ADVANCED
SCIENCE NEWS**
www.advancedsciencenews.com
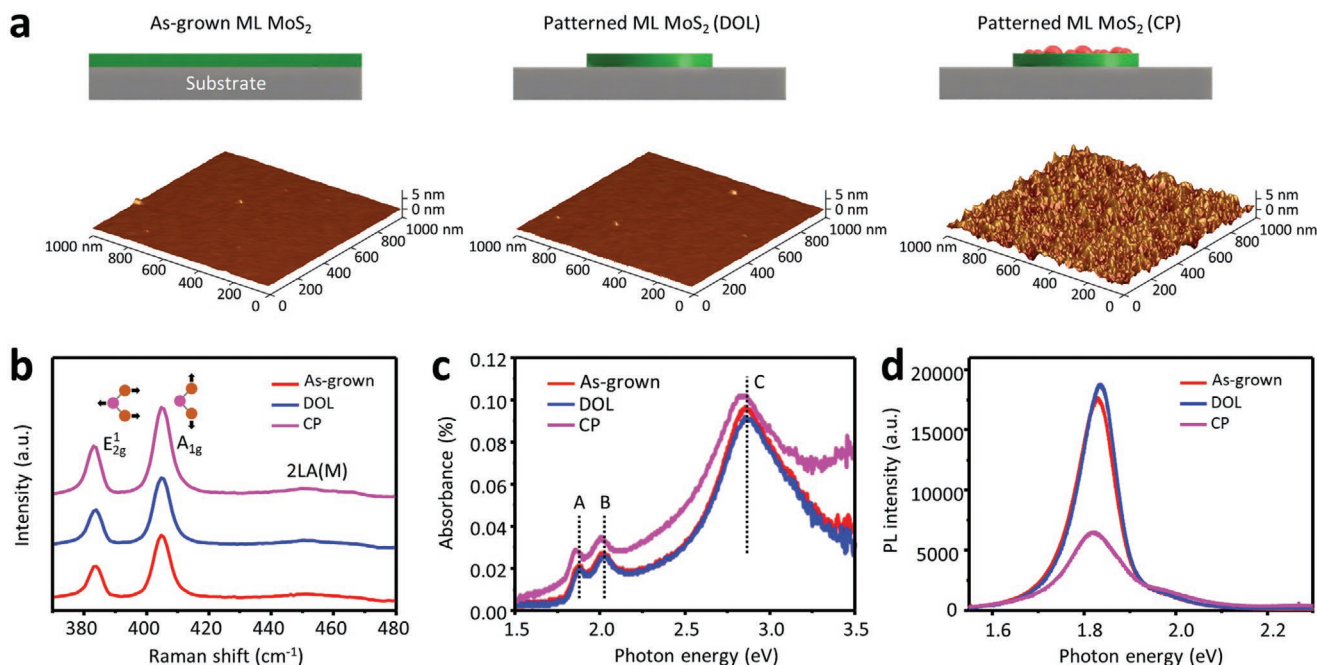
**ADVANCED
FUNCTIONAL
MATERIALS**
www.afm-journal.de

Figure 3. a) Schematics and AFM topography of as-grown, DOL, and CP MoS_2. b) Raman spectra with 514 nm laser excitation. No significant difference at intrinsic Raman modes (E^1_{2g}, A_{1g}) including 2LA(M) mode, related to the defect density. c) Absorption spectra with spatially filtered broadband light source. Peak position of all peaks of CP MoS_2 are slightly red-shifted, attributed that PR residues on CP MoS_2 decrease energy band gap and exciton binding energy by coulomb engineering. d) PL spectra with 532 nm excitation. PL intensity decreases significantly at photolithography-patterned samples compared other samples.

These characterizations confirmed that identical profiles were observed in all spots.

Optical characterization clearly confirms that DOL preserves pristine properties of vdW material unlike CP, so DOL is more beneficial for patterning vdW materials compared to CP. Moreover, DOL has competitive advantages over other focused-laser patterning methods with small power owing to highly intense photo source of DOL, the excimer laser. Thermal simulation reveals the advantages of DOL but, before revealing the advantages of DOL, mechanism of DOL is described to comprehend overall phenomenon in etching vdW materials of DOL as demonstrated below.

Figure 4 provides a DOL mechanism and FEM simulation analysis of material-dependent and substrate-dependent threshold power of DOL. Figure 4a exhibits SEM images of ML MoS_2 illuminated in various powers, including threshold power for etching (P_0), and the schematic illustration of SEM images. In DOL, partial etching of vdW materials occurred even under P_0, indicating that etching reactivity of ML MoS_2 to the photo source was dependent on spots, and etched regions were propagated from the initiated regions as illumination power increased. In Figure 4b, maximum temperatures in ML MoS_2, BL MoS_2, and graphene were calculated as 1579, 2639, and 1676 K under 25-ns-pulse illumination at 22.21, 18.66, and 31.73 mW cm^{-2}, respectively—the threshold power of each material. The calculated temperature was not sufficient to induce sublimation or laser ablation in ML MoS_2, but the temperature was sufficient to thermally decompose or oxidize materials in ambient air, as in previous studies.[27–29] Meanwhile, X-ray photoelectron spectroscopy (XPS) spectra in

Figure 4c indicate that Mo was totally removed by DOL, not forming an oxide in ML MoS_2. The results in Figure 4b,c, in line with prior experiments, show that Mo and S—with an insufficient number of chemical bonds in defect sites or edge sites of MoS_2—are thermally oxidized, and oxidized elements are then sublimated.[20,30] The size of the etched area increases as the process is repeated; thus, vdW materials are entirely etched through thermal decomposition. This phenomenon happened in DOL. Figure 4a shows that non-uniform etched areas, which are considered to be initiated from defects, were propagated as illumination power increased. Graphene was also etched through oxidation and oxide evaporation as indicated in a previous study.[31] The simulation result of graphene in Figure 4b supports this. Since the boiling temperature of graphene is significantly higher than simulated temperature and the decomposition temperature of graphene oxide is considerably lower than the simulated temperatures, thermal decomposition was considered to occur.[28,32,33] BL MoS_2 could be etched via laser ablation since its thermal stability is lower than ML $MoS2$, and the maximum temperature of BL MoS_2 was much higher than the boiling point.[20,27,29]

The threshold power for etching vdW materials in DOL depended on the type of materials and substrates, as described in **Table 2**. **Figure 5** elucidates the mechanism of material-, and substrate-dependent threshold power. Figure 5a shows simulated temperature of ML MoS_2, BL MoS_2, and graphene under identical illumination power of 18.66 MW cm^{-2}, as presented in the schematic illustration. Responsive temperature of ML MoS_2, BL MoS_2, and graphene were different (BL MoS_2 > ML MoS_2 > graphene) owing to different extinction coefficients or

**ADVANCED
SCIENCE NEWS**
www.advancedsciencenews.com

**ADVANCED
FUNCTIONAL
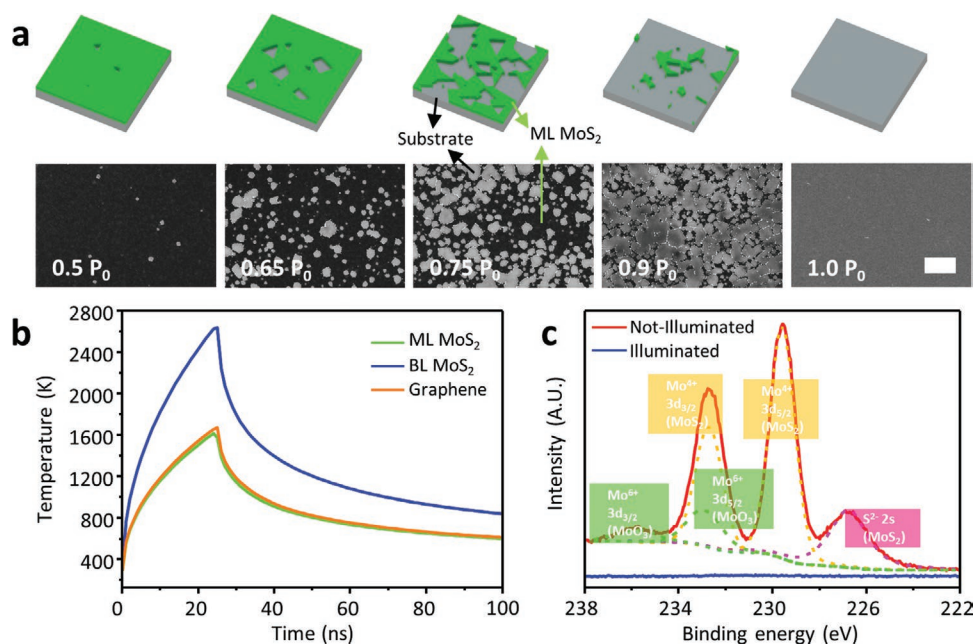MATERIALS**
www.afm-journal.de

Figure 4. a) SEM images of illuminated ML MoS$_2$ in various power and its schematic illustration. b) Temperature-versus-time plot of ML MoS$_2$, BL MoS$_2$, and GR under illumination at critical power for etching each material for 25 ns. c) XPS spectra of illuminated and not-illuminated ML MoS$_2$.

absorbances of materials. Cross-sectional simulation images of heat transport behaviors in Figure 5a indicate that the penetration depth of heat was shallow so that the impact of high temperature on substrates was small (Figure S12, Supporting Information). Figure 5b provides a trend of the threshold power and extinction coefficients of ML MoS$_2$, BL MoS$_2$, and graphene. The extinction coefficient, a parameter of light energy loss in specific materials, presents a trend opposite to that of the threshold power of ML MoS$_2$, BL MoS$_2$, and graphene. Even though other parameters, including volume, thermal constant, thermal stability, defect density, and surroundings, are important in the general thermal decomposition of materials,[31,34] extinction coefficient of materials is considered to play a major role in the threshold power in DOL.

Substrate-dependent threshold power was investigated in a system consisting of Al$_2$O$_3$ (mask), ML MoS$_2$ (target vdW material) on a substrate, and a 30-nm air gap between ML MoS$_2$ and Al$_2$O$_3$ (Figure 5c). FEM simulations were carried out with two substrates, quartz and PI. As there was higher heat distribution along the quartz substrate with its higher thermal conductivity (1.46 W mK^{-1}), lesser heat remained in ML MoS$_2$ and the temperature of ML MoS$_2$ was relatively low (1579 K). In contrast, there was lesser heat distribution along the PI substrate due to the relatively low thermal conductivity (0.166 W mK^{-1}), and in this case, heat was more isolated in ML MoS$_2$, inducing a

higher temperature of ML MoS$_2$ on the PI substrate (3500 K). The differing thermal conductivity of quartz and PI caused different heat distribution profiles in the substrates under illumination at the same power, 22.21 MW cm^{-2}. Therefore, the substrate-dependent threshold power was attributed to different thermal conductivity levels of the substrates.

Figure 6 describes a comparative simulation with two different illumination power of P$_0$ (threshold power to entirely etch ML MoS$_2$ on a quartz substrate in DOL, 22.21 MW cm^{-2}) and P$_0$/20 in ML MoS$_2$ system to comprehend the advantage of the photo source in DOL. The photo source in this work has a relatively high power density (5.29–58.19 MW cm^{-2}) in short pulse (25 ns) compared to other photo sources.[12,14] The simulation was carried out in the system where light was blocked in the region covered by circular Al pattern with radius of 5 μm in the sapphire mask (remarked as the black-dotted line circle in Figure 6a) and light reached ML MoS$_2$ in the rest of regions. In the P$_0$/20 case, it took 95 μs to reach the temperature, 1579 K, where ML MoS$_2$ was entirely etched in the P$_0$ case (Figure S13, Supporting Information). This longer illumination in the P$_0$/20 case made the different result with that of the P$_0$ case. As shown in Figure 6a, thermal responses of masked and illuminated regions were exactly distinguishable following the Al pattern (black-dotted line circle) in the P$_0$ case. On the other hand, in the P$_0$/20 case, moderate temperature gradient was formed between masked and illuminated regions and thermal responses of masked and illuminated regions were not precisely separated. This behavior in the P$_0$/20 case was induced by heat distribution along ML MoS$_2$ owing to longer illumination time and indicates that highly intensive light with short pulse allowed precise pattern of ML MoS$_2$ following Al patterns of the sapphire mask in DOL. Moreover, in the P$_0$ case, temperature of the masked region approached ≈420 K that is even lower than gentle annealing temperature of ML MoS$_2$ in

Table 2. Threshold power of ML MoS$_2$, BL MoS$_2$, and graphene on quartz and PI substrates.

	PI	Quartz
ML MoS$_2$	10.58 MW cm^{-2}	22.21 MW cm^{-2}
ML MoS$_2$	5.29 MW cm^{-2}	18.66 MW cm^{-2}
Graphene	14.81 MW cm^{-2}	31.73 MW cm^{-2}

**ADVANCED
SCIENCE NEWS**

www.advancedsciencenews.com
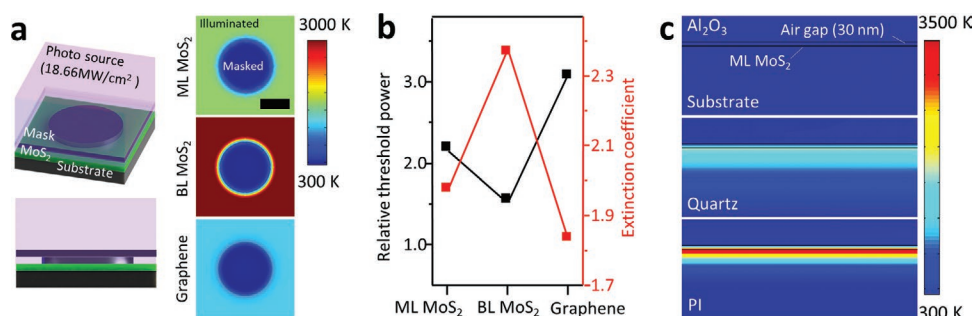
**ADVANCED
FUNCTIONAL
MATERIALS**

www.afm-journal.de

Figure 5. a) Schematic illustration of illuminated process and temperature simulation images of ML MoS$_2$, BL MoS$_2$, and GR with a scale bar of 5 µm. b) Graphs of relative critical power and extinction coefficients of ML MoS$_2$, BL MoS$_2$, and GR. c) Simulated images of heat distribution of mask-covered ML MoS$_2$ on quartz and PI substrates.

other works,[1,35] but, in the P$_0$/20, the temperature approached ≈1100 K that can induce severe sulfur vacancies or oxidation in MoS$_2$.[30,36] Higher temperature in the masked region of the P$_0$/20 case were caused by heat transport from the illuminated region to the masked region during the illumination as illustrated in Figure 6b. These results in Figure 6a,b indicate that the highly intensive light used in this work is critical to pattern vdW materials in high resolution without the negative effect on residual regions.

For further comprehension of the advantage of the photo source in this work, the simulation with the illumination power of P$_0$/50 was carried out in ML MoS$_2$ on a quartz substrate (Figure 6c). Unlike the responsive temperature in the P$_0$ case (1579 K), a responsive temperature in the P$_0$/50 case was saturated at 966 K and did not increase even under a tremendously long illumination time (999 µs) as described in Figure 6d. The reason why the responsive temperature in the P$_0$/50 case was saturated is that heat was dissipated through the substrate before enough heat, induced by the illumination, could accumulate. With the assumption that ML MoS$_2$ is entirely etched at a critical temperature, a high-power-density photo source is required to facilitate the etching phenomenon in ML MoS$_2$. If the power is lower than the critical value, ML MoS$_2$ will not be entirely etched, as sufficient heat is not accumulated in ML MoS$_2$.

3. Conclusion

In conclusion, the DOL patterning of various 2D vdW materials (ML MoS$_2$, BL MoS$_2$, graphene, ML WSe$_2$, and 2D MOF) was demonstrated with high-throughput, multiscale, and high-resolution features. VdW materials were patterned regardless of pattern shape, scale and the type of substrates which vdW materials were on. DOL provided clean surface of ML MoS$_2$ after patterning unlike CP produced photoresist residues on the ML MoS$_2$, which are known to induce negative effects on contact resistance and properties of vdW materials. Optical investigation revealed that DOL did not accompany modification of optical and electrical properties, which was exhibited in CP samples. Simulation results indicated that the highly intense photo source used in this work was critically required for high resolution patterning without degradation of vdW materials. In addition, we expect that our DOL can be applied to

other 2D materials, such as, 2D perovskites and 2D oxides.[37,38] Through the DOL demonstrations of 2D vdW materials, we anticipate that our DOL method will provide a new research platform for applications—from semiconductor processes to bio-engineering.

4. Experimental Section

Preparation of Various Van der Waals Materials: MoS$_2$ and WSe$_2$ films were grown on various substrates via metal-organic chemical vapor deposition. The equipment consisted of a quartz tube (4.3 inches in diameter) with a 3-zone heating furnace system. Mo(CO)$_6$ (Sigma-Aldrich 577 766), (C$_2$H$_5$)$_2$S (Sigma-Aldrich 107 247), W(CO)$_6$ (Sigma-Aldrich 472 956), and (CH$_3$)$_2$Se (Alfa Aesar 593-79-3) were used as precursors. For the MoS$_2$ growth, Mo(CO)$_6$ and (C$_2$H$_5$)$_2$S were injected in the reaction system at the flow rates of 0.6 and 0.4 sccm, respectively, through a mass flow controller with the aid of the dilution gas, Ar (800 Torr). In addition to the precursor gases, additional Ar and H$_2$ were also injected in the system at the flow rates of 5 and 1000 sccm, respectively. The reaction was then carried out at a growth temperature of 600 °C at 3.1 Torr for 14 h. For the WSe$_2$ growth, W(CO)$_6$ and (CH$_3$)$_2$Se were injected in the reaction system at the flow rates of 4 and 0.2 sccm, respectively, through a mass flow controller with the aid of the dilution gas, Ar (800 Torr). In addition to precursor gases, additional Ar and H$_2$ were also injected in the system at the flow rates of 5 and 1400 sccm, respectively. The reaction was then carried out at the growth temperature of 600 °C at 3.3 Torr for 14 h. In both cases, the NaCl-containing plate was placed in the system to enhance morphology and crystallinity of materials.[35,39]

The as-prepared MoS$_2$ and WSe$_2$ were transferred to other substrates via poly(methyl methacrylate) (PMMA, Sigma-Aldrich 200 336) and DI. PMMA was spin-coated on the as-grown samples, and after annealing at 170 °C for 2 min, the samples were slowly dipped in DI. PMMA-coated MoS$_2$ and WSe$_2$ were then floated on the surface of DI, and the floated films were scooped by substrates that MoS$_2$ and WSe$_2$ were to be transferred. After scooping, the samples were annealed at 180 °C for 10 min and dipped in acetone overnight to remove PMMA. The samples were then cleaned with IPA and DI for 10 min each, and residual solvents were dried with a nitrogen gun.

For transfer of MoS$_2$ and WSe$_2$ to a chitosan substrate, both materials were floated on DI without PMMA and were scooped by the chitosan substrate.

For PL measurement, ML MoS$_2$ was directly grown on a quartz substrate and characterized without transferring it to maintain the original properties.

Graphene on Cu foil was purchased from LG electronics, and it was transferred to desired substrates following a method. PMMA was spin-coated on the graphene and the sample was dipped in 0.5 M (NH$_4$)$_2$S$_2$O$_8$ (Sigma-Aldrich 248 614) aqueous solution at 60 °C for 2 h to etch the Cu
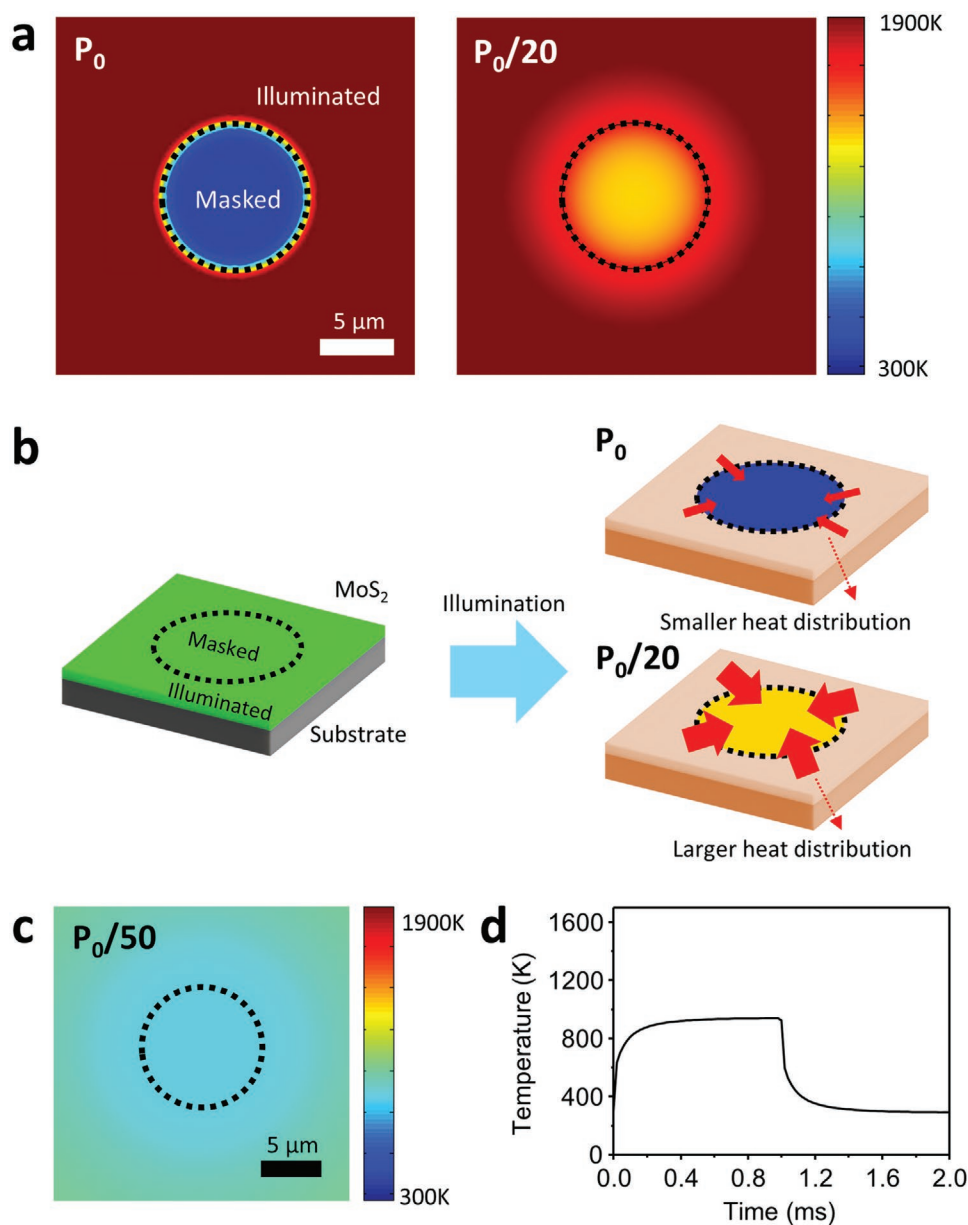
Figure 6. a) Simulation results of heat response of ML MoS_2 under the power of P_0 and $P_0/50$. b) Schematic illustration of different heat transport behaviors of illuminated ML MoS_2 under the power of P_0 and $P_0/50$. c) Simulation result and d) time versus temperature plot of heat response of ML MoS_2 under the power of $P_0/50$.

foil. The PMMA-suspended graphene was then delaminated from the Cu foil and placed on the surface of the solution. The film was transferred to a desired substrate using a lift-off technique.

2D MOF was synthesized using a liquid/air interfacial method, following a previous study.[40] ZnTPyP (Sigma-Aldrich 52 718), the ligand in the MOF, at a concentration of 0.2 mM, was dissolved in a solvent consisting of methanol and dichloromethane at a ratio of 1:3. Then, 20 µL of the resultant ZnTPyP solution was injected into an interface between air and DI-water-based solution containing 10 mM $Cu(NO_3)_2$ (Sigma-Aldrich 223 395) to provide ZnTPyP ligands with Cu^{2+} ions. The MOF film that formed on the surface was then transferred to a desired substrate using a lift-off technique.

Chitosan films were fabricated following the reference with modification.[41] Chitosan powder (Sigma-Aldrich 448 869) were dissolved in DI for 10 wt% and, after mixing, acetic acid (Sigma-Aldrich

695 092) were added to the solution for 10 wt%. As-prepared solution was poured into solid plastic dish and dried at 70 °C for overnight.

Preparation of Sapphire Mask: Sapphire substrates with a thickness of 420 µm were sonicated in acetone, IPA, and distilled water for 10 min each and dried with the aid of a nitrogen gun. Photoresist (PR, AZ 5214E, AZ Electronic Materials) patterns were prepared on as-cleaned sapphire samples through CP, and Al was deposited on these samples for 30 nm via a sputter (SRN-110, SORONA). The samples were then developed in KWIK remover for 12 h and rinsed in distilled water and IPA for 10 min each to fully remove the developer. After rinsing, the samples were dried utilizing a nitrogen gun.

To fabricate submicron-scale masks, PMMA patterns were prepared via E-Beam Lithography System (JBX-9300FS, JEOL Ltd.) on cleaned substrates, and Al was deposited on the samples via a sputter. A lift-off was then performed in acetone at room temperature for 1 h. The as-prepared samples were then rinsed in IPA and DI.

Direct Optical Lithography Process: For the DOL patterning of the vdW materials, a XeCl excimer laser system (Coherent COMPex Pro 205, wavelength of 308 nm, pulse duration of 25 ns) was used. The laser, emitted from a mixture of xenon and chlorine gas under 22 kV extraction voltage and high-pressure conditions, was used to illuminate the samples with the materials and masks, which were held together using adhesive tape (810R, 3M) to decrease the gap between the photomask and vdW materials as much as possible in ambient conditions. The beam spot has a square shape with a size of 625 $\mu m^2 \times 625\ \mu m^2$. All the laser process parameters, including beam spot size, repetition rate, and stage movement rate, were kept constant except for its power density, which varied between 5.29 and 58.19 MW cm^{-2}, depending on materials and substrates. Photomasks used for multiple experiments after rinsing with DI water. The schematic of the illumination system used in this research is illustrated in Figure S14, Supporting Information

Patterning through Conventional Photolithography: PR patterns were made on vdW materials via standard photolithography, and exposed regions of the vdW materials were etched in SF_6/O_2 plasma through reactive ion etching. The samples were lifted off to acetone at 70 °C overnight to remove photoresist patterns. They were then rinsed in IPA and DI, consecutively, for 10 min to remove acetone, and the residual solution was dried by nitrogen gun blowing.

Characterizations (Optical Microscope, Scanning Electron Microscopy, Raman, Ellipsometer, X-Ray Photoelectron Spectroscopy, Atomic Force Microscope, I–V Measurement): The centimeter-scale optical images were observed through a smartphone camera and the micron-scale optical images of patterned vdW materials and sapphire mask were observed through an optical microscope (OM, BX53M, OLYMPUS). SEM (S-4800, HITACHI) was used to characterize the submicron-scale morphology of the ML MoS_2 patterns and mask. Removal of vdW materials was confirmed by Raman spectroscopy (ARAMIS, Horiba Jobin Yvon, France). Thickness and optical parameters of materials were measured by ellipsometer (Woollam, M2000D (RCT)). Removal of Mo-containing materials was confirmed by XPS (Sigma Probe, Thermo VG Scientific). AFM (INNOVA-LABRAM HR800, Horiba Jobin & Bruker) was employed to measure the surface roughness of samples. The *I–V* characteristic of electrical devices was measured by a parameter analyzer system (4200A-SCS, Keithley).

Two-Terminal Device Fabrication: Electrode-shape shadow masks were attached to as-patterned BL MoS_2 through DOL and CP using an adhesive tape. Cr/Au (10/30 nm) were deposited on samples via e-beam evaporation.

Absorption Measurement: The UV–vis absorption spectra of As-grown, DOL, and PR-patterned MoS_2 in air at room temperature were extracted by measuring transmission and reflection spectrum at once. Light source was 300 W Xenon lamp (ORIEL Instruments), spatially filtered by 100 um pin hole, and collimated with diameter of ≈10 um on sample via ×10 objective lens. The transmitted and reflected light were collimated again to fiber-coupled MAYA2000 PRO spectrometer (Ocean Optics).

Micro-PL Experiments: Room temperature micro-PL spectra and Raman spectroscopy of As-grown, DOL, and PR-patterned MoS_2 were carried out with continuous-wave DPSS 532 nm laser (Shanghai Dream Lasers Technology Co.) with the power attenuation to 50 uW via neutral density filter were used for excitation source. Emission were collected via ×10 objective lens and dispersed by the monochromator (Teledyne Princeton Instruments, IsoPlane SCT320) coupled with CCD detector (Teledyne Princeton Instruments, PIXIS 400).

Finite Element Method Simulation: Optical responses of materials were simulated using the transfer matrix method. The input beam was assumed to be normally incident with a uniform intensity. Moreover, the incident light is a superposition of pulses with slight differences in resonance wavelength, so it was assumed that the incident excimer laser was a rectangular pulse with a 25-ns pulse width. The absorbed optical power density was calculated by $\omega \varepsilon''|E|^2/2$, where $|E|^2$ is the intensity of the electric field, ω is the frequency of the incident light, and ε'' is the imaginary part of the dielectric function. All the properties of the materials were measured by an ellipsometer. The calculated power density was applied in the thermal simulation as the heat source. The time-dependent temperature distribution was then simulated by solving heat transport equations using the FEM (COMSOL Multiphysics). Periodic boundary conditions were set for the side boundaries, and the temperature of the top and bottom boundaries were fixed at 300 K. The top and bottom boundaries were placed sufficiently far (≈40 μm) from the absorbing layers, and thus, the resulting temperature distribution does not vary depending on the vertical size of the simulation region.

Supporting Information

Supporting Information is available from the Wiley Online Library or from the author.

Conflict of Interest

The authors declare no conflict of interest.

Data Availability Statement

Research data are not shared.

[1] Y. Wang, J. C. Kim, R. J. Wu, J. Martinez, X. Song, J. Yang, F. Zhao, A. Mkhoyan, H. Y. Jeong, M. Chhowalla, *Nature* **2019**, *568*, 70.

[2] L. A. Jauregui, A. Y. Joe, K. Pistunova, D. S. Wild, A. A. High, Y. Zhou, G. Scuri, K. de Greve, A. Sushko, C.-H. Yu, T. Taniguchi, K. Watanabe, D. J. Needleman, M. D. Lukin, H. Park, P. Kim, J. A. Paulson, *Science* **2019**, *366*, 870.

[3] C. Song, G. Noh, T. S. Kim, M. Kang, H. Song, A. Ham, M. K. Jo, S. Cho, H. J. Chai, S. R. Cho, K. Cho, J. Park, S. Song, I. Song, S. Bang, J. Y. Kwak, K. Kang, *ACS Nano* **2020**, *14*, 16266.

[4] J. Jang, H. Kim, S. Ji, H. J. Kim, M. S. Kang, T. S. Kim, J. E. Won, J. H. Lee, J. Cheon, K. Kang, W. B. Im, J. U. Park, *Nano Lett.* **2020**, *20*, 66.

[5] E. Park, M. Kim, T. S. Kim, I. S. Kim, J. Park, J. Kim, Y. Jeong, S. Lee, I. Kim, J. K. Park, G. T. Kim, J. Chang, K. Kang, J. Y. Kwak, *Nanoscale* **2020**, *12*, 24503.

[6] J. Liang, K. Xu, B. Toncini, B. Bersch, B. Jariwala, Y. C. Lin, J. Robinson, S. K. Fullerton-Shirey, *Adv. Mater. Interfaces* **2019**, *6*, 1801321.

[7] L. Sun, L. Lin, Z. Wang, D. Rui, Z. Yu, J. Zhang, Y. Li, X. Liu, K. Jia, K. Wang, L. Zheng, B. Deng, T. Ma, N. Kang, H. Xu, K. S. Novoselov, H. Peng, Z. Liu, *Adv. Mater.* **2019**, *31*, 1902978.

[8] J. Choi, H. Zhang, H. Du, J. H. Choi, *ACS Appl. Mater. Interfaces* **2016**, *8*, 8864.

[9] J. H. Kim, J. Lee, J. H. Kim, C. C. Hwang, C. Lee, J. Y. Park, *Appl. Phys. Lett.* **2015**, *106*, 251606.

[10] Y. Guo, P. C. Shen, C. Su, A. Y. Lu, M. Hempel, Y. Han, Q. Ji, Y. Lin, E. Shi, E. McVay, L. Dou, D. A. Muller, T. Palacios, J. Li, X. Ling, J. Kong, *Proc. Natl. Acad. Sci. USA* **2019**, *116*, 3437.

[11] X. Chen, Y. J. Park, T. Das, H. Jang, J. B. Lee, J. H. Ahn, *Nanoscale* **2016**, *8*, 15181.

[12] L. Lin, J. Li, W. Li, M. N. Yogeesh, J. Shi, X. Peng, Y. Liu, B. B. Rajeeva, M. F. Becker, Y. Liu, D. Akinwande, Y. Zheng, *Adv. Funct. Mater.* **2018**, *28*, 1803990.

[13] V. Shautsova, S. Sinha, L. Hou, Q. Zhang, M. Tweedie, Y. Lu, Y. Sheng, B. F. Porter, H. Bhaskaran, J. H. Warner, *ACS Nano* **2019**, *13*, 14162.

[14] X. Liu, S. T. Howell, A. Conde-Rubio, G. Boero, J. Brugger, *Adv. Mater.* **2020**, *32*, 2001232.

[15] P. Zhao, R. Wang, D. H. Lien, Y. Zhao, H. Kim, J. Cho, G. H. Ahn, A. Javey, *Adv. Mater.* **2019**, *31*, 1900136.

[16] K. F. Mak, K. He, C. Lee, G. H. Lee, J. Hone, T. F. Heinz, J. Shan, *Nat. Mater.* **2013**, *12*, 207.

[17] X. Wu, C. Shu, X. He, S. Wang, X. Fan, Z. Yu, D. Yan, W. Huang, *Macromol. Chem. Phys.* **2020**, *221*, 1900506.

[18] H. Teng, K. Koike, D. Zhou, Z. Satoh, Y. Koike, Y. Okamoto, *J. Polym. Sci., Part A: Polym. Chem.* **2009**, *47*, 315.

[19] D. Chen, H. G. Zachmannt, *Polymer* **1991**, *32*, 1612.

[20] X. Wang, W. Fan, Z. Fan, W. Dai, K. Zhu, S. Hong, Y. Sun, J. Wu, K. Liu, *Nanoscale* **2018**, *10*, 3540.

[21] Y. Zhong, B. R. Cheng, C. Park, A. Ray, S. Brown, F. Mujid, J. U. Lee, H. Zhou, J. Suh, K. H. Lee, A. J. Mannix, K. Kang, S. J. Sibener, D. A. Muller, J. Park, *Science* **2019**, *366*, 1379.

[22] A. Raja, A. Chaves, J. Yu, G. Arefe, H. M. Hill, A. F. Rigosi, T. C. Berkelbach, P. Nagler, C. Schüller, T. Korn, C. Nuckolls, J. Hone, L. E. Brus, T. F. Heinz, D. R. Reichman, A. Chernikov, *Nat. Commun.* **2017**, *8*, 15251.

[23] H. J. Conley, B. Wang, J. I. Ziegler, R. F. Haglund, S. T. Pantelides, K. I. Bolotin, *Nano Lett.* **2013**, *13*, 3626.

[24] K. Greben, S. Arora, M. G. Harats, K. I. Bolotin, *Nano Lett.* **2020**, *20*, 2544.

[25] S. Mignuzzi, A. J. Pollard, N. Bonini, B. Brennan, I. S. Gilmore, M. A. Pimenta, D. Richards, D. Roy, *Phys. Rev. B* **2015**, *91*, 195411.

[26] J. Feng, X. Qian, C. W. Huang, J. Li, *Nat. Photonics* **2012**, *6*, 866.

[27] I. G. Vasilyeva, R. E. Nikolaev, *J. Alloys Compd.* **2008**, *452*, 89.

[28] E. Ganz, A. B. Ganz, L. M. Yang, M. Dornfeld, *Phys. Chem. Chem. Phys.* **2017**, *19*, 3756.

[29] Y. Zhang, D. Zhang, J. Wu, Z. He, X. Deng, *AIP Adv.* **2017**, *7*, 075010.

[30] H. Zhou, F. Yu, Y. Liu, X. Zou, C. Cong, C. Qiu, T. Yu, Z. Yan, X. Shen, L. Sun, B. I. Yakobson, J. M. Tour, *Nano Res.* **2013**, *6*, 703.

[31] J. R. Hahn, H. Kang, S. M. Lee, Y. H. Lee, *J. Phys. Chem. B* **1999**, *103*, 9944.

[32] J. Wang, J. Huang, R. Yan, F. Wang, W. Cheng, Q. Guo, J. Wang, *J. Mater. Chem. A* **2015**, *3*, 3144.

[33] F. Najafi, M. Rajabi, *Int. Nano Lett.* **2015**, *5*, 187.

[34] P. Chen, W. Xu, Y. Gao, P. Holdway, J. H. Warner, M. R. Castell, *J. Phys. Chem. C* **2019**, *123*, 3876.

[35] K. Kang, S. Xie, L. Huang, Y. Han, P. Y. Huang, K. F. Mak, C. J. Kim, D. Muller, J. Park, *Nature* **2015**, *520*, 656.

[36] J. Wu, H. Li, Z. Yin, H. Li, J. Liu, X. Cao, Q. Zhang, H. Zhang, *Small* **2013**, *9*, 3314.

[37] M. Kang, H. Chai, H. B. Jeong, C. Park, I. Jung, E. Park, M. M. Çiçek, I. Lee, B.-S. Bae, E. Durgun, J. Y. Kwak, S. Song, S.-Y. Choi, H. Y. Jeong, K. Kang, *ACS Nano* **2021**, *15*, 8715.

[38] H. R. Rasouli, J. Kim, N. Mehmood, A. Sheraz, M. Jo, S. Song, K. Kang, T. S. Kasirga, *Nano Lett.* **2021**, *21*, 3997.

[39] S. Xie, L. Tu, Y. Han, L. Huang, K. Kang, K. U. Lao, P. Poddar, C. Park, D. A. Muller, R. A. Distasio, J. Park, *Science* **2018**, *359*, 1131.

[40] R. Makiura, O. Konovalov, *Dalton Trans.* **2013**, *42*, 15931.

[41] P. Cazón, M. Vázquez, *Environ. Chem. Lett.* **2020**, *18*, 257.